Supporting Information

Tunable Chiral Optics in All-Solid-Phase Reconfigurable Dielectric Nanostructures

Jingang Li[1], Mingsong Wang[1,2], Zilong Wu[1], Huanan Li[2], Guangwei Hu[2,3], Taizhi Jiang[4], Jianhe Guo[1], Yaoran Liu[1,5], Kan Yao[1], Zhihan Chen[1], Jie Fang[1], Donglei Fan[1], Brian A. Korgel[4], Andrea Alù[2*], and Yuebing Zheng[1,5*]

[1] Materials Science & Engineering Program, Texas Materials Institute, and Walker Department of Mechanical Engineering, The University of Texas at Austin, Austin, TX, USA.

[2] Photonics Initiative, Advanced Science Research Center and Graduate Center, City University of New York, New York, NY, USA.

[3] Department of Electrical and Computer Engineering, National University of Singapore, Singapore, Singapore.

[4] McKetta Department of Chemical Engineering, The University of Texas at Austin, Austin, TX, USA.

[5] Department of Electrical and Computer Engineering, The University of Texas at Austin, Austin, TX, USA.

* E-mail: zheng@austin.utexas.edu (Y.Z.), aalu@gc.cuny.edu (A.A.)

Contents

Experimental Details

Sample preparation. CTAC was purchased from Chem-Impex. CTAC solution was prepared by dissolving 0.8 g CTAC powder in 5 mL isopropyl alcohol (IPA). 40 μL CTAC solution was spin coated on to a glass substrate to form a thin layer of CTAC solid film after IPA evaporation. SiNPs and SiNWs diluted in ethanol or deionized water were spin coated on CTAC film for the assembly experiments.

Synthesis of SiNPs. The synthesis of the hydrogen-terminated amorphous SiNPs was previously reported.[1] Trisilane and *n*-hexane were added to a 10 mL titanium reactor in a nitrogen-filled globe box (**Caution**: Trisilane is a pyrophoric liquid and the glove box oxygen concentration needs to be below 1 ppm). The size of the SiNPs was determined by the amount of trisilane, and the amount of *n*-hexane was chosen from its phase diagram at target reaction temperature to maintain a pressure of 34.5 Mpa. In this work, 42 μL trisilane was used in each reaction and the resulting SiNP diameter is ~500nm. For a typical reaction at 420°C, 5.9 mL of *n*-hexane was used. After sealed, the reactor was transferred from the glove box to a heating block, heated to the target temperature for 10 min for complete decomposition of the trisilane, and cooled down to room temperature by an ice bath. Then, the SiNPs were washed with chloroform by centrifuging at 8000 rpm for 5 min for three times. The precipitate was collected and dispersed in chloroform before use. The hydrogen concentration in the SiNPs was tuned by the reaction temperature. The SiNPs used in this work have a hydrogen concentration of ~35 at.%.

Fabrication of SiNWs. SiNWs were fabricated via a metal-assisted chemical etching (MACE) method as previously discussed.[2] In brief, a catalytic metal thin film with circular nanoholes was fabricated by nanosphere lithography and used as the mask. Undoped silicon wafers (University Wafer) with the orientation of <100> and a resistance larger than ohm·cm was used. The silicon wafer and metal mask were immersed into the etchant composed of 4.7 M hydrofluoric acid and 0.3 M hydrogen peroxide to dissolve the silicon underneath the metal film to leave arrays of nanowires. Finally, metal etchants were

used to remove the catalytic metal layer, followed by sonication in DI water to break the nanowires off the substrate. The nanowires used in this study are ~5 μm in length and ~170 nm in diameter.

Optical setup and measurement. An inverted microscope (Nikon TiE) with an oil objective (Nikon, ×100, NA 0.5–1.3) and a motorized stage was used for the assembly experiments. A 532 nm laser (Coherent, Genesis MX STM-1 W) was expanded with a 5× beam expander (Thorlabs, GBE05-A) and directed to the microscope. An oil dark-field condenser (NA 1.20–1.43) was used to focus the white illuminating light onto the sample from the top. The forward scattering signal from the sample was directed to a spectrometer (Andor) with a 500 nm grating. A linear polarizer and a quarter waveplate (Thorlabs) were used to transform unpolarized white light into circularly polarized light. Background spectra were recorded and subtracted to obtain the scattering signal of the target nanostructures. The scattering spectra were normalized by the incident light, e.g., $S_{\mathrm{RCP/LCP}} = \frac{I^{Scat}_{\mathrm{RCP/LCP}} - I^{Back}_{\mathrm{RCP/LCP}}}{I^{in}_{\mathrm{RCP/LCP}}}$, where S_{RCP} and S_{LCP} are the scattering spectra at RCP and LCP, $I^{Scat}_{\mathrm{RCP/LCP}}$, $I^{Back}_{\mathrm{RCP/LCP}}$, and $I^{in}_{\mathrm{RCP/LCP}}$ are the measured intensity of the scattering light, background, and the incident light at RCP/LCP, respectively. Circular differential scattering (CDS) spectra were calculated the by $S_{\mathrm{RCP}} - S_{\mathrm{LCP}}$. It is worth noting that the measurement is rotationally symmetric in the two-dimensional (2D) plane. Thus, and 2D rotation of the substrate and the orientation of the SiNW will not alter the measurement results, which simplifies the assembly process.

Chiral sensing. For the chiral sensing experiments, a LH and a RH structure were assembled separately on the same substrate. After measuring their chiroptical responses, the sample was slowly put into water or IPA to remove the CTAC layer to avoid affecting the sensing. Then, the sample was immersed with DI water and the solution of chiral molecules (two enantiomers) to measure the CDS spectra. Between each measurements, the sample was soaked in ethanol for 10 minutes and rinsed with water and ethanol for three times to remove the residue molecules.

SEM characterizations. All SEM images were taken with a FEI Quanta 650 SEM.

Numerical simulations. Simulations of scattering and CDS spectra were performed via finite-difference time-domain (FDTD) method (Lumerical FDTD). The geometries of Si nanowires and nanospheres were set as cylinders with flat-faced ends and standard spheres, respectively. Both the SiNP and SiNW are placed at the substrate with a gap of 20 nm. The mesh size was determined as 5 nm by convergence testing. The nanostructures were placed on a glass substrate with the ambient environment set as CTAC (n = 1.38). The incident circularly polarized light has an incident angle of 69°. To simulate dark-field setup, the scattering spectra were obtained by averaging the results from four different azimuthal angles (0°, 90°, 180°, 270°). It should be noted that, since the experimental measurement region was 1.8 × 1.8 μm^2, a homebuilt MATLAB program was employed to extract the scattering intensities of corresponding regions based on simulation results. The CDS spectra of the regions of interest were finally calculated by simulating the localized scattering intensities under LCP and RCP excitations, respectively. The near-field distribution was monitored both at the cross-sectional plane of the SiNW passing through the center of the SiNP and at the normal plane of the incident light.

Supporting Notes

Note S1. Mie theory and multipole decomposition.

The scattering spectra and multipole decomposition in Figure 2c,d are obtained using Mie theory for a sphere and for an infinite cylinder, respectively.[3, 4] The scattering cross-section Q_{sct} of a dielectric sphere of radius r and refractive index n contains contributions from the multipolar Mie resonances, which are either electric (a_l) or magnetic (b_l) by nature:

$$Q_{sct} = \frac{2}{(kr)^2}\sum_{l=1}^{\infty}(2l+1)(|a_l|^2 + |b_l|^2), \tag{1}$$

where k is the wavenumber and l denotes the index of the multipoles. The Mie coefficients a_l and b_l can be expressed in the following form

$$a_l = \frac{R_l^{(a)}}{R_l^{(a)} + iT_l^{(a)}}, \tag{2a}$$

$$b_l = \frac{R_l^{(b)}}{R_l^{(b)} + iT_l^{(b)}}, \tag{2b}$$

where R_l and T_l are both complex-valued functions:

$$R_l^{(a)} = n\psi_l'(kr)\psi_l(nkr) - \psi_l(kr)\psi_l'(nkr), \tag{3a}$$

$$T_l^{(a)} = n\chi_l'(kr)\psi_l(nkr) - \chi_l(kr)\psi_l'(nkr), \tag{3b}$$

$$R_l^{(b)} = n\psi_l'(nkr)\psi_l(kr) - \psi_l(nkr)\psi_l'(kr), \tag{4a}$$

$$T_l^{(b)} = n\chi_l(kr)\psi_l'(nkr) - \chi_l'(kr)\psi_l(nkr). \tag{4b}$$

Here, $\psi_l(x) = \sqrt{\frac{\pi x}{2}}J_{l+1/2}(x)$ and $\chi_l(x) = \sqrt{\frac{\pi x}{2}}Y_{l+1/2}(x)$, with $J_{l+1/2}(\cdot)$ and $Y_{l+1/2}(\cdot)$ being the Bessel and Neumann functions and prime denoting derivative.

The scattering by a cylinder is dependent on the polarization of the incident light. By denoting the Mie coefficients associated with *p*-polarized component of the incidence (i.e., electric field perpendicular

to the cylinder's axis) as a_l, and those associated with *s*-polarized component (i.e., electric field parallel to the cylinder's axis) as b_l, the scattering cross-section Q_{sct} of a cylinder of radius r and refractive index n is given by

$$Q_{sct} = \frac{2}{kr}(|a_0|^2 + 2\sum_{l=1}^{\infty}|a_l|^2 + |b_0|^2 + 2\sum_{l=1}^{\infty}|b_l|^2), \tag{5}$$

where

$$a_l = \frac{nJ_l(nkr)J_l'(kr) - J_l'(nkr)J_l(kr)}{nJ_l(nkr)H_l^{(1)\prime}(kr) - J_l'(nkr)H_l^{(1)}(kr)}, \tag{6a}$$

$$b_l = \frac{J_l(nkr)J_l'(kr) - nJ_l'(nkr)J_l(kr)}{J_l(nkr)H_l^{(1)\prime}(kr) - nJ_l'(nkr)H_l^{(1)}(kr)}, \tag{6b}$$

and $J_l(\cdot)$ and $H_l^{(1)}(\cdot)$ are the Bessel function and Hankel function of the first kind, respectively. For circularly polarized incident light, both a_l and b_l can be excited, as shown in Figure 2d.

Note S2. Coupled mode theory analysis.

As elaborated in the main text, the scattering in our nanostructure is modelled by the CMT:[5]

$$\frac{d\boldsymbol{a}}{dt} = (i\Omega - \Gamma)\boldsymbol{a} + D(\theta)^T|S_+\rangle \tag{7}$$

$$|S_-\rangle = K(\theta)|S_+\rangle + D(\theta)\boldsymbol{a} \tag{8}$$

where $|S_+\rangle = \begin{pmatrix} e_x^+ \\ e_y^+ \\ e_0^+ \end{pmatrix}$ and $|S_-\rangle = \begin{pmatrix} e_x^- \\ e_y^- \\ e_0^- \end{pmatrix}$ describe the input and output respectively, and for our experimental interest, $\begin{pmatrix} e_x^+ \\ e_y^+ \end{pmatrix}$ is identified to be the Jones vector for the incoming light from the source and e_0^- is the scattered light to the detector with $|e_0^-|^2$ for its intensity. Inspired from the Born-Kuhn model

of a chiral molecule,[6-9] the coupling matrix $D(\theta)$ for the chiral nanostructure is constructed as $D(\theta) = \begin{pmatrix} ice^{-i\theta} & 0 \\ 0 & ice^{i\theta} \\ c_1 & c_2 \end{pmatrix}$, where the coefficients c, c_1, and c_2 are real, and the effective phase θ depends on the relative positions of the SiNP and the SiNW. Furthermore, to satisfy the relationship[5]

$$KD^* = -D \tag{9}$$

we simply set $K(\theta) = \mathrm{diag}(e^{-i2\theta}, e^{i2\theta}, -1)$ and assume that Eq. (9) is not affected by the presence of the intrinsic (material and radiation) loss in our system.[10, 11] The total decay matrix $\Gamma = \begin{pmatrix} \gamma_1 & \gamma \\ \gamma & \gamma_2 \end{pmatrix}$, incorporating the intrinsic losses $\Gamma_0 = \mathrm{diag}(\gamma_{10}, \gamma_{20})$, can be related to the coupling matrix D as:[12]

$$\Gamma = \Gamma_0 + \frac{1}{2} D^+ D = \begin{pmatrix} \gamma_{10} + \frac{1}{2}(c^2 + {c_1}^2) & \frac{1}{2} c_1 c_2 \\ \frac{1}{2} c_1 c_2 & \gamma_{20} + \frac{1}{2}(c^2 + {c_2}^2) \end{pmatrix}. \tag{10}$$

Solving Equations 7 and 8, we have the output light:

$$\left| S_- \right\rangle = \left[K + D \frac{1}{i(\omega I_2 - \Omega) + \Gamma} D^T \right] \left| S_+ \right\rangle, \tag{5}$$

and for our experiment $e_0^+ = 0$, we get the wave amplitude e_0^- towards the detector:

$$e_0^- = (c_1 \quad c_2) \frac{1}{i(\omega I_2 - \Omega) + \Gamma} \begin{pmatrix} ice^{-i\theta} & \\ & ice^{i\theta} \end{pmatrix} \begin{pmatrix} e_x^+ \\ e_y^+ \end{pmatrix} \equiv V(\omega) \begin{pmatrix} e_x^+ \\ e_y^+ \end{pmatrix} \tag{6}$$

where I_2 is the 2×2 identity matrix. For the left-handed circularly polarized (LCP) light, $\begin{pmatrix} e_x^+ \\ e_y^+ \end{pmatrix} = \frac{1}{\sqrt{2}}\begin{pmatrix} 1 \\ -i \end{pmatrix} \equiv |L\rangle$, and $\begin{pmatrix} e_x^+ \\ e_y^+ \end{pmatrix} = \frac{1}{\sqrt{2}}\begin{pmatrix} 1 \\ i \end{pmatrix} \equiv |R\rangle$ for the right-handed circularly polarized (RCP) light. The circular differential scattering (CDS) can be expressed as:[8]

$$\mathrm{CDS} \equiv \ln\left|e_{0\ \mathrm{RCP}}^{-}\right|^2 - \ln\left|e_{0\ \mathrm{LCP}}^{-}\right|^2 = \ln\frac{|V(\omega)|R\rangle|^2}{|V(\omega)|L\rangle|^2} \tag{7}$$

$$\mathrm{CDS} \equiv \ln\frac{[cos\theta(A_1 - B_2) + sin\theta(A_2 - B_1)]^2 + [cos\theta(A_2 + B_1) - sin\theta(A_1 + B_2)]^2}{[cos\theta(A_1 + B_2) + sin\theta(A_2 + B_1)]^2 + [cos\theta(A_2 - B_1) - sin\theta(A_1 - B_2)]^2} \tag{8}$$

where $A_1 = c_1\left(\gamma_{20} + \frac{c^2 - {c_2}^2}{2}\right)$, $A_2 = c_1(\omega - \omega_0) + c_2\xi$, $B_1 = c_2\left(\gamma_{10} + \frac{c^2 - {c_1}^2}{2}\right)$, and $B_2 = c_2(\omega - \omega_0) + c_1\xi$. Note that when the phase difference θ is 0, the system becomes achiral and CDS = 0 for the whole frequency regime. This requirement imposes further the constrains $A_1 = B_1 = 0$ from Equation 8, and thus ${c_2}^2 = {c_1}^2 - 2(\gamma_{10} - \gamma_{20})$ and $c^2 = {c_1}^2 - 2\gamma_{10}$. Consequently, CDS can be written as:

$$\mathrm{CDS} \equiv \ln\frac{{A_2}^2 + {B_2}^2 - 2A_2B_2sin2\theta}{{A_2}^2 + {B_2}^2 + 2A_2B_2sin2\theta} \tag{9}$$

From Equation 9, we have $\mathrm{CDS}(\theta) = -\mathrm{CDS}(-\theta)$. Since LH and RH structures have opposite phase difference, this equation agrees well with the experimental and numerical results. We obtained γ_{10} and γ_{20} from the simulated scattering spectra of the SiNP and SiNW and fitted the simulated CDS curves with ω_0, c_1, and ξ as the fitting parameters. The curves fitted by CMT are well consistent with the numerical simulations (Figure 4b), indicating that the optical chirality results from the coupling between resonance modes in the SiNP and SiNW, which is further determined by the phase difference between two components.

Supporting Figures

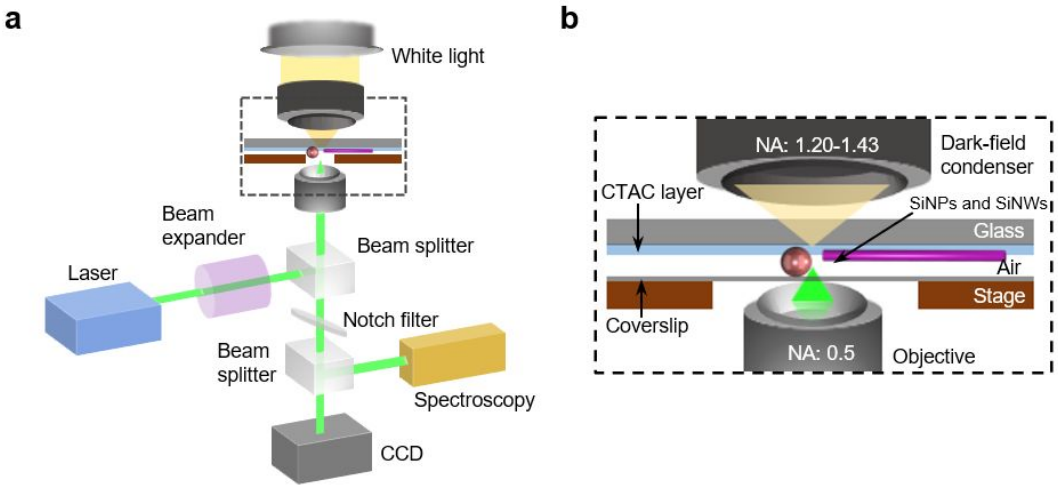

Figure S1. Experimental setup. a) The optical setup for the assembly of chiral nanostructures on solid substrates. b) Detailed setup of sample configurations and dark-field scattering measurement. SiNPs and SiNWs were dispersed on a glass substrate coated with a thin layer of solid CTAC for the manipulation and assembly experiments.

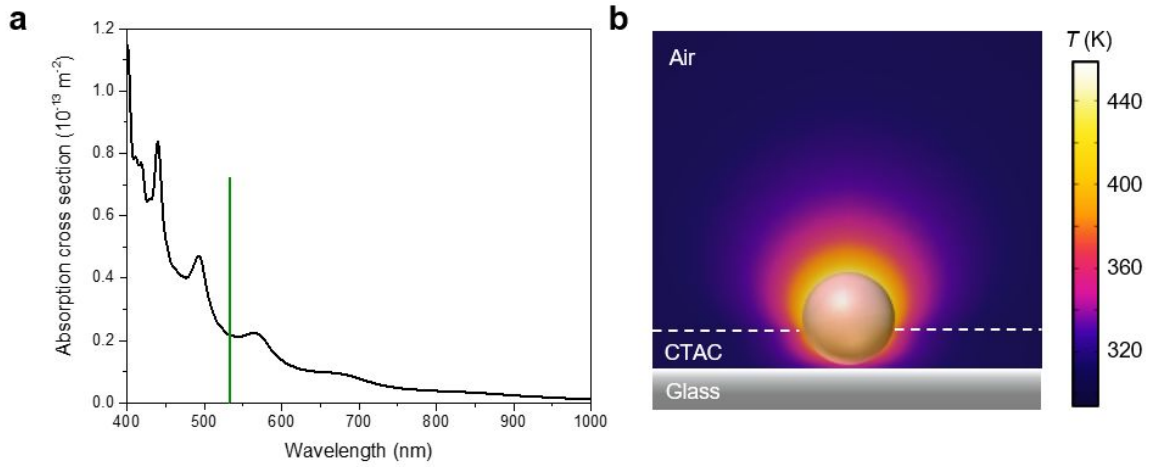

Figure S2. Optothermal response of the hydrogenated amorphous SiNPs. a) Simulated absorption spectrum of a 500 nm hydrogenated amorphous SiNP. The green line represents the wavelength of the laser beam. b) Simulated temperature distribution around a 500 nm SiNP. Incident power intensity: 2 mW μm^{-2}. SiNPs are known to be efficient light-absorbing particles to convert light to heat.[13] This simulation shows a strong absorption band at the wavelength shorter than ~600 nm. Meanwhile, the absorption loss is very low at the longer wavelength owing to its dielectric features. When the laser irradiates the SiNP, the temperature can rise to higher than 450K at a low optical power, which will cause the order-disorder transition of CTAC around the SiNP.

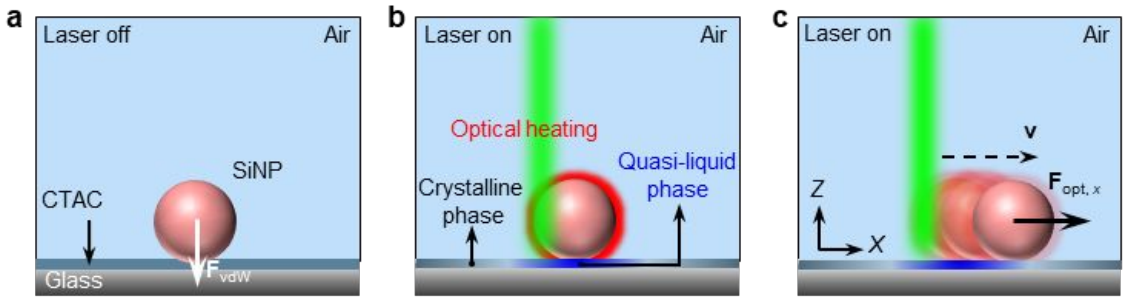

Figure S3. Detailed mechanisms for the optical manipulation of SiNPs on solid substrates. a) CTAC is in its solid phase under room temperature. The SiNP adheres to the CTAC film with van der Waals forces. b) When the laser is on, optical heating of the SiNP produces a large amount of heat and results in a large temperature rise around the SiNP (Figure S2b). The surrounding CTAC around the SiNP undergoes a localized order-disorder transition and transforms into a quasi-liquid phase,[14] which significantly eliminates the van der Waals friction forces between the SiNP and CTAC layer. c) The SiNP is nudged away from the laser beam with optical scattering forces. Through steering the laser beam or moving the substrate with a motorised stage, SiNPs can be dynamically transported to any target position.

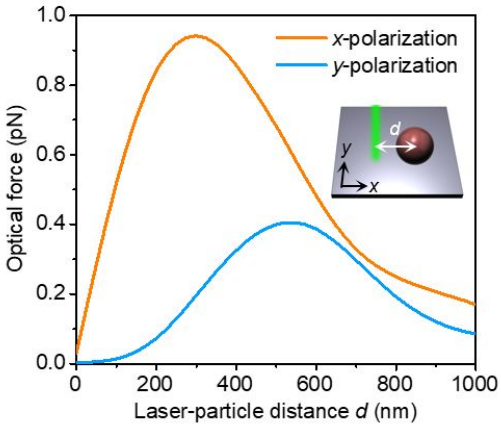

Figure S4. Simulated optical forces on a 500 nm SiNP as a function of laser-particle distance. For both *x*- and *y*- polarization, the optical force nudges the particle away against the laser beam. Thus, optical forces can push the SiNP under any polarizations, which enables the effective manipulation of SiNPs in all directions on the substrate Incident power intensity: 4 mW μm^{-2}.

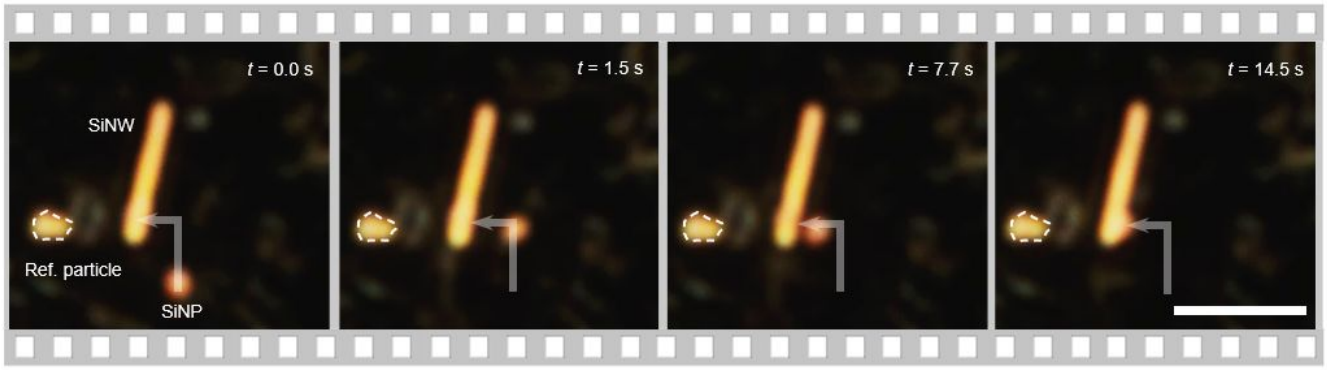

Figure S5. Sequential dark-field optical images showing real-time construction of chiral structures with a SiNP and a SiNW. The white arrows depict the path. Scale bar: 5 μm.

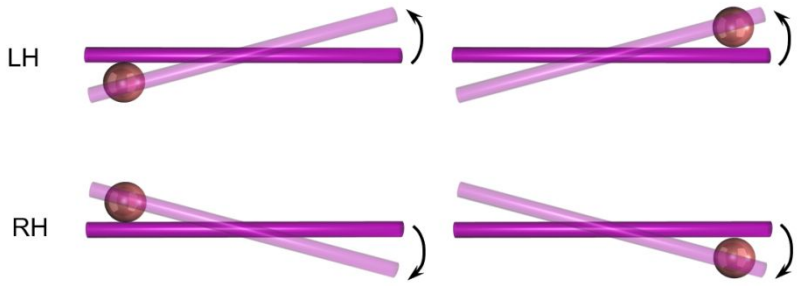

Figure S6. Convention of the handedness of the assembled chiral nanostructures. The chiral nanostructures composed of a SiNW and a SiNP beside one end of the nanowire. A left-handed (LH) structure refers to the case where the SiNW can sweep over the SiNP by rotating the SiNW about its center anticlockwise at a small angle (< 90 degree). In a right-handed (RH) structure, the SiNW can sweep over the SiNP by rotating the SiNW about its center clockwise at a small angle (< 90 degree).

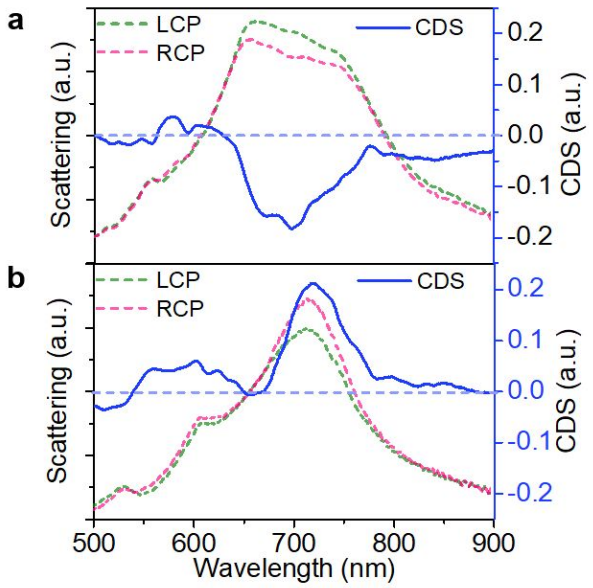

Figure S7. Measured scattering spectra under RCP and LCP illumination and the corresponding circular differential scattering spectra of (a) LH structure in Figure 1c and (b) RH structure in Figure 1d.

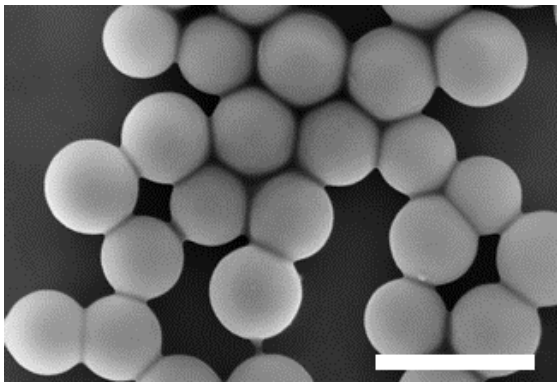

Figure S8. SEM image of colloidal SiNPs. Chemically synthesized SiNPs used in this study have very good spherical shape. The diameter is around 500 nm with slight deviations. The scale bar is 1 μm.

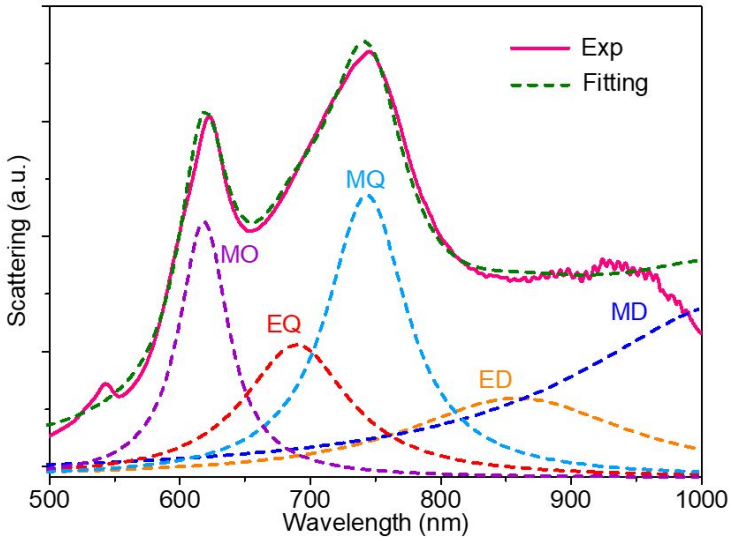

Figure S9. Fitting for the experimental spectrum of a 500 nm SiNP. The pink solid line is the experimental spectra in Figure 2a. The green dashed line shows the fitting summary and other dashed lines are the fitting peaks for different modes. The dark blue, orange, light blue, red, and purple dashed lines correspond to magnetic dipole, electric dipole, magnetic quadrupole, electric quadrupole, and magnetic octupole resonance modes, respectively. The fitting results are in good match with the multipole decomposition calculations.

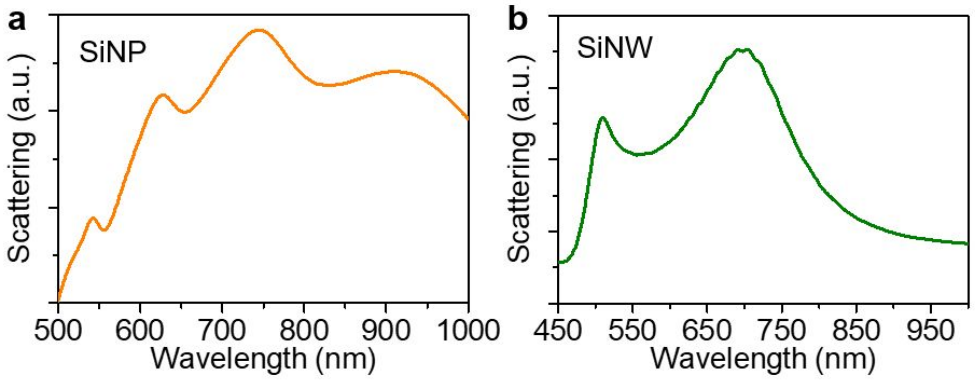

Figure S10. FDTD simulation of the scattering spectra of a single (a) SiNP and (b) SiNW in Figure 2.

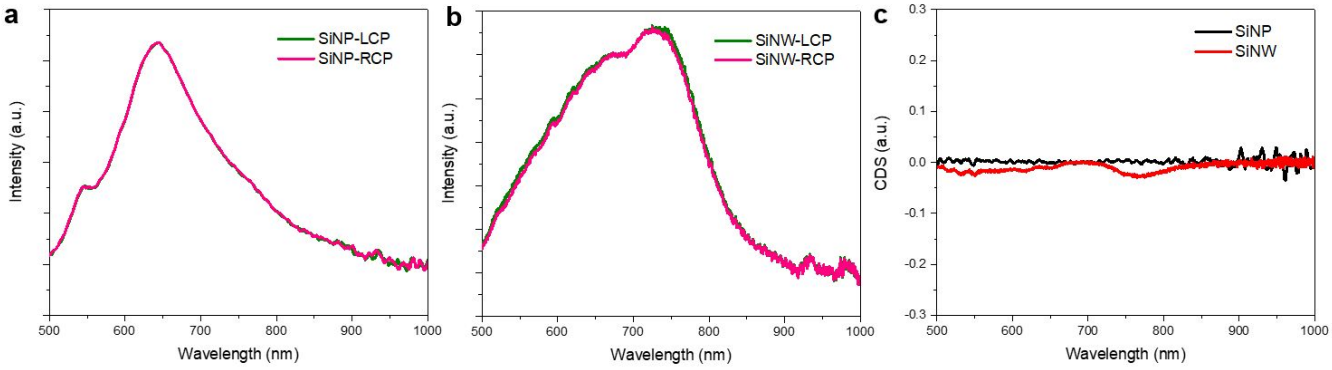

Figure S11. Spectral characterization of individual building blocks in Figure 3. a,b) Measured scattering spectra of (a) single SiNP and (b) single SiNW under LCP and RCP light. c) CDS spectra of the single SiNP and SiNW. The single dielectric components show negligible chiroptical response in the far-field scattering spectra due to their symmetric geometries (sphere and cylinder).

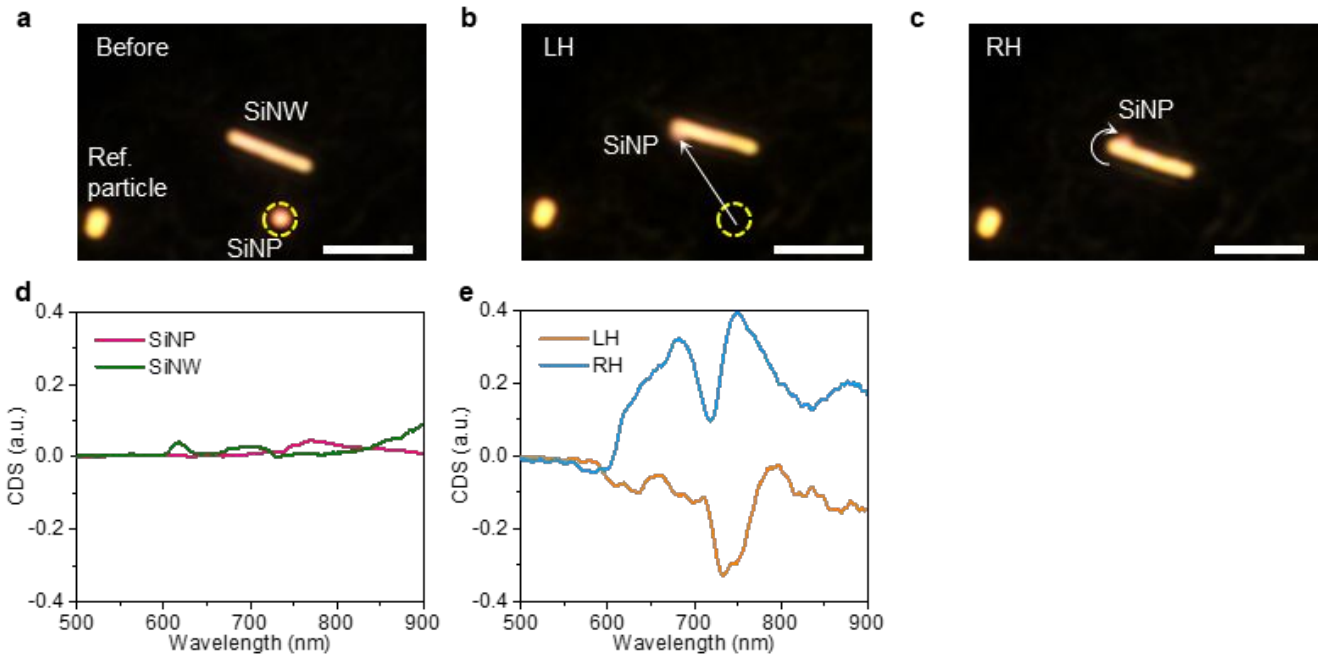

Figure S12. Another example of reconfigurable chiral nanostructures on a solid substrate. a-c) Dark-field optical images of (a) a SiNP and a SiNW before assembly, (b) the assembled LH structure, and (c) the assembled RH structure. d) Measured CDS spectra of the single SiNP and SiNW. Similar to Figure S11, the single dielectric components show negligible chiroptical response. e) Measured CDS spectra of the assembled LH and RH structures. This result demonstrates that the handedness of the chiral nanostructures can be switch by simply moving the SiNP form one side to the other side of the SiNW.

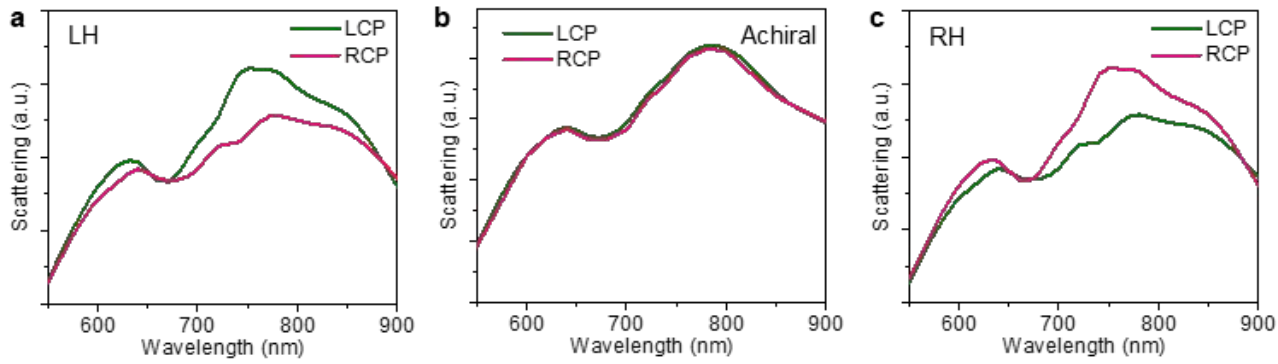

Figure S13. Simulated scattering spectra of (a) LH, (b) achiral, and (c) RH structure under LCP and RCP light.

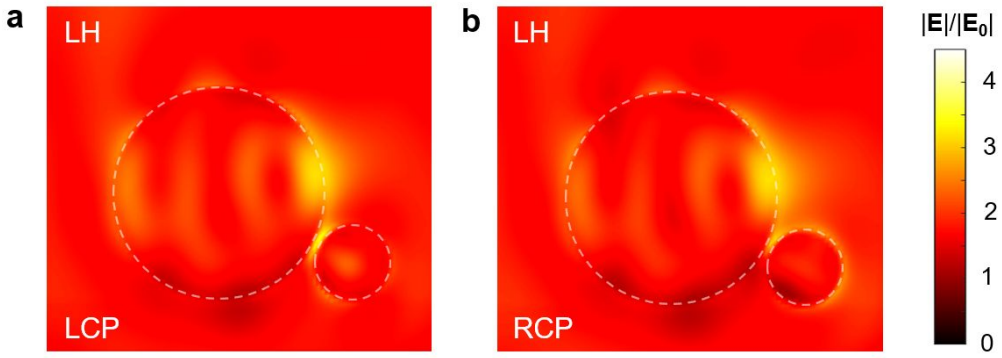

Figure S14. Simulated electric field distributions scattering in the LH structure at 620 nm under (a) LCP and (b) RCP incidence. All electric field distributions are cut at the cross-sectional plane of the SiNW passing through the center of the SiNP. A more pronounced hotspot at the gap between the SiNP and SiNW can be observed for the LH structure at LCP incidence.

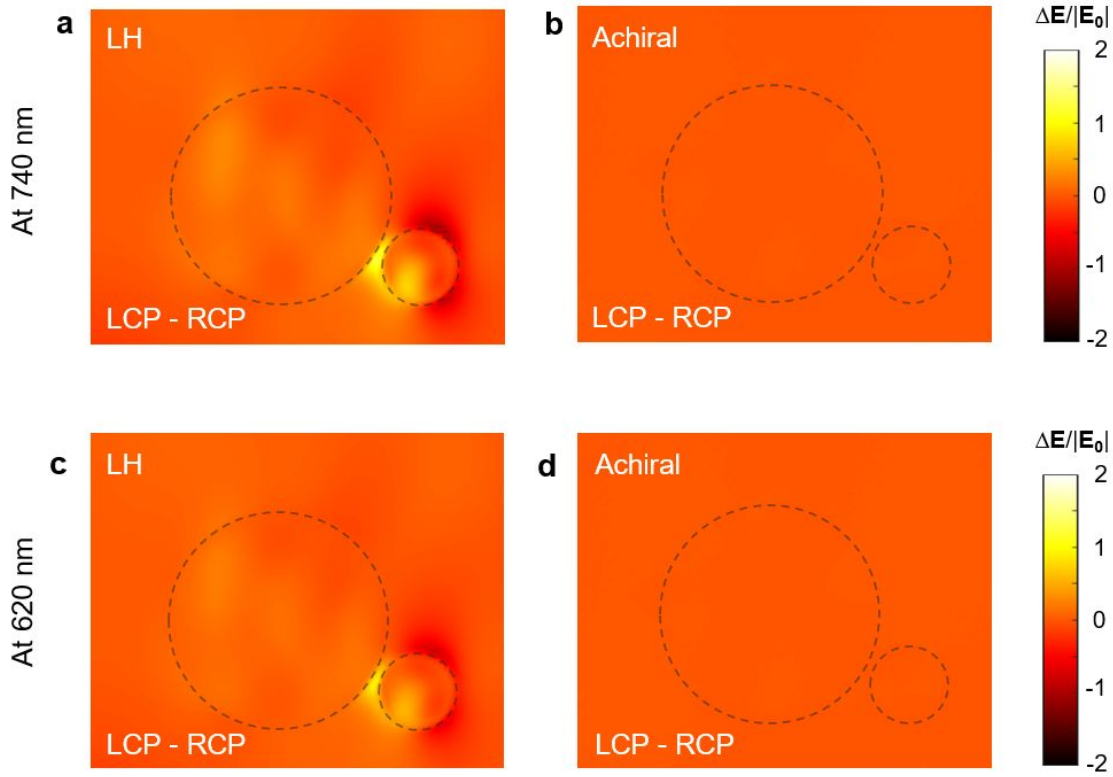

Figure S15. The simulated differential electric field distributions. a,c) Differential electric field distributions in the LH structure at (a) 740 nm and (c) 620 nm. b,d) Differential electric field distributions in the achiral structure at (b) 740 nm and (d) 620 nm. Clearly, for the LH structure, a positive hotspot can be observed at the gap between the SiNP and SiNW, while for the achiral structure, no obvious difference between the LCP and RCP incidence can be distinguished.

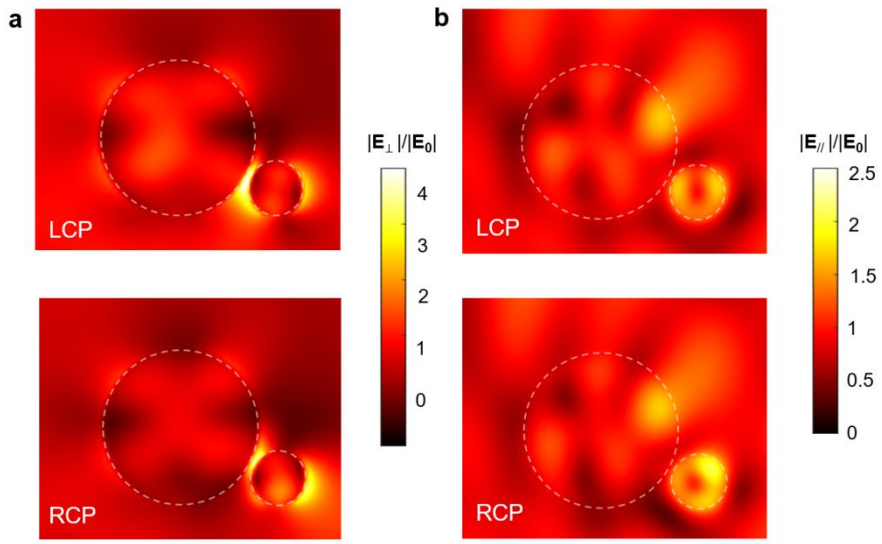

Figure S16. Simulated in-plane electric field components mapping in the LH structure at 740 nm. Electric field components (a) perpendicular to the SiNW ($E_{\perp}$) and (b) parallel to the SiNW ($E_{//}$) under LCP and RCP incidence.

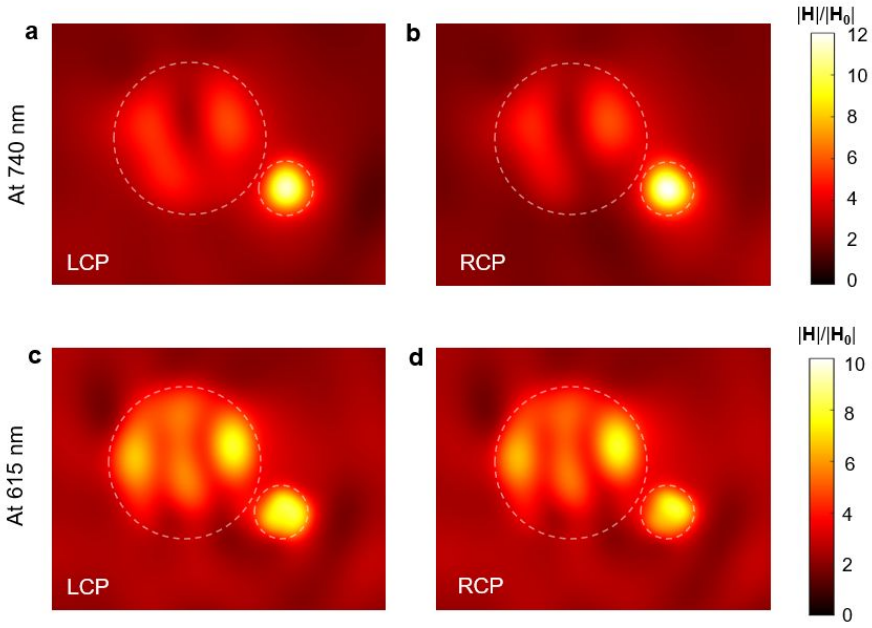

Figure S17. Magnetic field enhancement mapping in the LH structure. a,b) Magnetic field distribution at 740 nm under (a) LCP and (b) RCP illumination. c,d) Magnetic field distribution at 620 nm under (c) LCP and (d) RCP illumination.

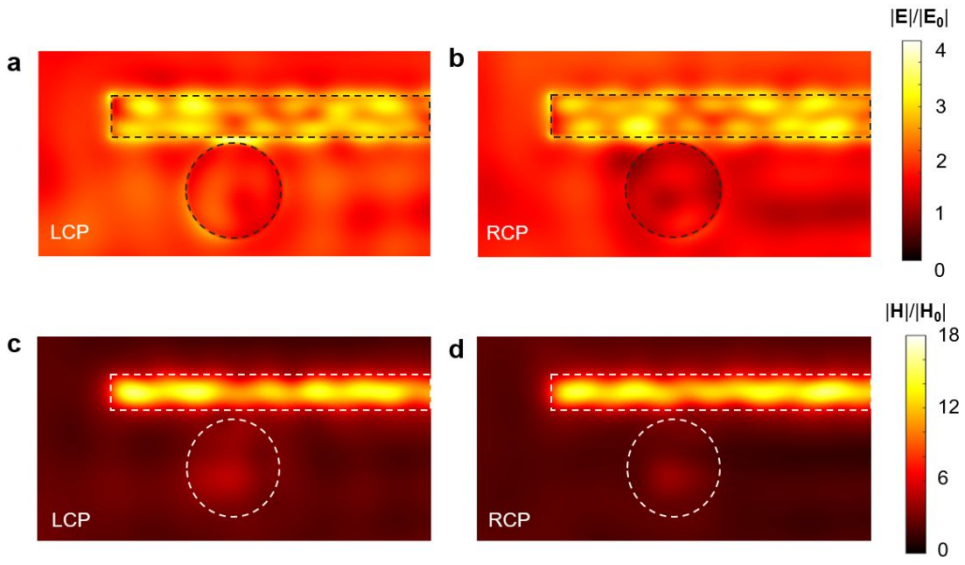

Figure S18. Electric and Magnetic field mapping in the LH structure cut at the normal plane to the incident direction. a,b) Electric field distribution at 740 nm under (a) LCP and (b) RCP illumination. c,d) Magnetic field distribution at 740 nm under (c) LCP and (d) RCP illumination. For the electric field, there is a brighter hotspot at the SiNP-SiNW gap under the LCP illumination compared with RCP incidence, which is consistent with the results in Figure 4c,d. Dielectric materials are known to support strong magnetic field enhancement. The LH structure show strong magnetic field enhancement under both LCP and RCP incidence with a maximum enhancement factor larger than 18. No obvious asymmetric response is observed. Most magnetic fields are confined in the materials, with some extending out.

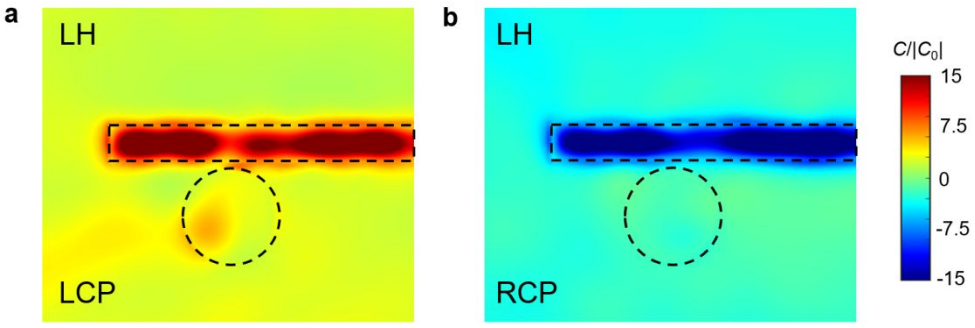

Figure S19. Optical chirality mapping in the LH structure at 740 nm under (a) LCP and (b) RCP illumination.

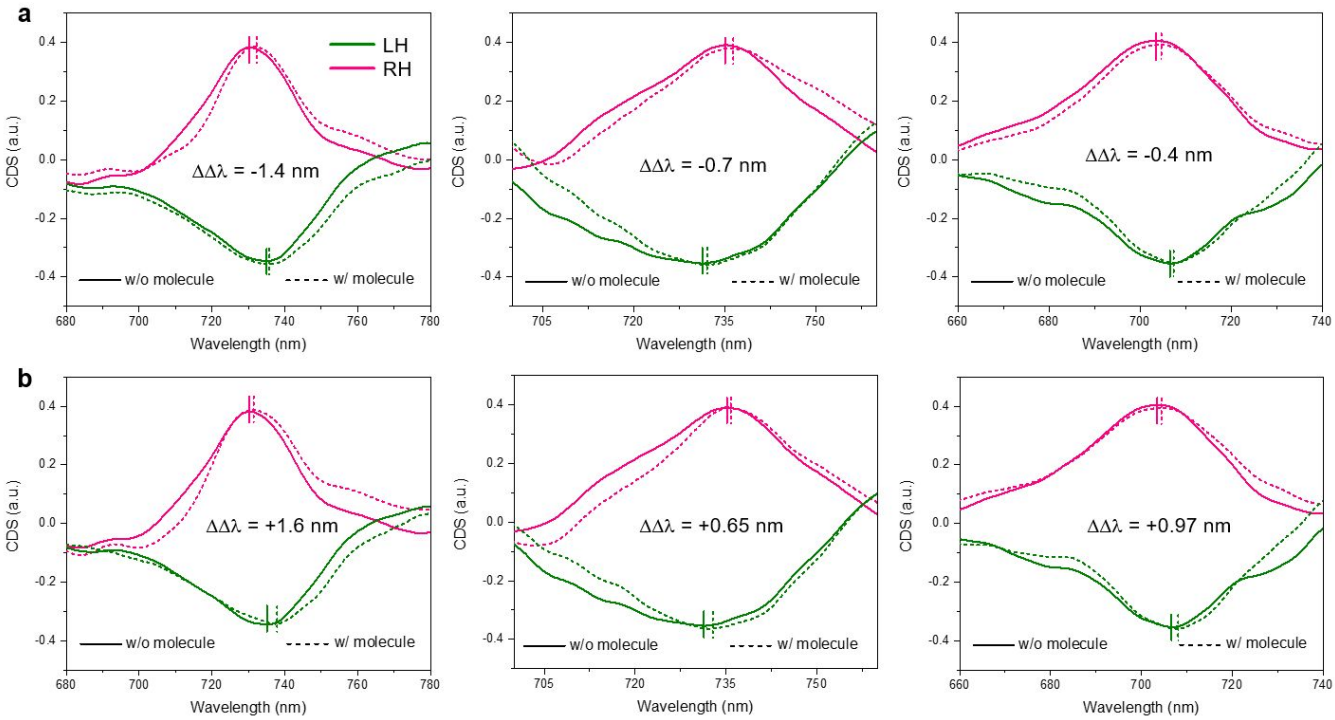

Figure S20. Measured CDS peak shifts in LH and RH structures induced by the adsorption of (a) L-Phenylalanine and (b) D-Phenylalanine.

References

(1) Harris, J. T.; Hueso, J. L.; Korgel, B. A. Hydrogenated Amorphous Silicon (a-Si:H) Colloids. *Chem. Mater.* **2010,** *22*, 6378-6383.

(2) Liang, Z.; Teal, D.; Fan, D. Light Programmable Micro/Nanomotors with Optically Tunable in-Phase Electric Polarization. *Nat. Commun.* **2019,** *10*, 5275.

(3) Cihan, A. F.; Curto, A. G.; Raza, S.; Kik, P. G.; Brongersma, M. L. Silicon Mie Resonators for Highly Directional Light Emission from Monolayer MoS_2. *Nat. Photonics* **2018,** *12*, 284-290.

(4) Savelev, R. S.; Sergaeva, O. N.; Baranov, D. G.; Krasnok, A. E.; Alù, A. Dynamically Reconfigurable Metal-Semiconductor Yagi-Uda Nanoantenna. *Phys. Rev. B* **2017,** *95*, 235409.

(5) Wonjoo, S.; Zheng, W.; Shanhui, F. Temporal Coupled-Mode Theory and the Presence of Non-Orthogonal Modes in Lossless Multimode Cavities. *IEEE Journal of Quantum Electronics* **2004,** *40*, 1511-1518.

(6) Born, M. The Natural Optical Activity of Liquids and Gases. *Phys. Z* **1915,** *16*, 251.

(7) Kuhn, W. Quantitative Relationships for Natural Optical Activity. *Phys Chem B* **1929,** *4*, 14-36.

(8) Yin, X.; Schäferling, M.; Metzger, B.; Giessen, H. Interpreting Chiral Nanophotonic Spectra: The Plasmonic Born–Kuhn Model. *Nano Lett.* **2013,** *13*, 6238-6243.

(9) Svirko, Y. P.; Zheludev, N. I., *Polarization of Light in Nonlinear Optics*. John Wiley & Sons: New York, 2000.

(10) Krasnok, A.; Baranov, D.; Li, H.; Miri, M.-A.; Monticone, F.; Alú, A. Anomalies in Light Scattering. *Adv. Opt. Photon.* **2019,** *11*, 892-951.

(11) Sweeney, W. R.; Hsu, C. W.; Stone, A. D. Theory of Reflectionless Scattering Modes. *arXiv preprint arXiv:1909.04017* **2019**.

(12) Fan, S.; Suh, W.; Joannopoulos, J. D. Temporal Coupled-Mode Theory for the Fano Resonance in Optical Resonators. *J. Opt. Soc. Am. A* **2003,** *20*, 569-572.

(13) Lin, L.; Kollipara, P. S.; Kotnala, A.; Jiang, T.; Liu, Y.; Peng, X.; Korgel, B. A.; Zheng, Y. Opto-Thermoelectric Pulling of Light-Absorbing Particles. *Light: Sci. Appl.* **2020,** *9*, 34.

(14) Tian, Y. C.; Yu, J.; Gu, M.; Lian, Y. D.; Ai, X. Q.; Tang, T. B. Impedance Spectroscopic Study on Rotator and Disordered Phases in Trimethylammonium Chlorides. *J. Phys. Chem. C* **2016,** *120*, 23905-23909.